

Constraining the Formation Time and Depth of Magnetic Sources within the Martian Crust

Version 1 (Initial submission, 01/29/2023)

Abstract

There's compelling evidence to suggest Mars once had a rich atmosphere and large bodies of surface water which may have hosted life. The primary reason Mars lost these was because of the demise of its planetary magnetic field, or dynamo. The precise timing of the dynamo's demise is still debated, with estimates ranging from 4.2 Ga to 3.0 Ga. Large meteor impacts offer a unique window into the dynamo's earliest history as they involve the sudden heating/compression of surface iron-bearing minerals, introducing a thermal and shock wave remanent magnetization which reflects the background field at the time of formation and can be preserved for billions of years. Here, we analyze newly acquired high-resolution magnetometer data from NASA's MAVEN orbiter in/around craters between 70-500 km diameter, then contextualize the impact in Mars's geological history through crater-density techniques. Out of 857 total craters that fit these constraints, we only find 24 that exhibit clear impact-induced demagnetization, suggesting the magnetic layer is deeply buried. The earliest case of unambiguous (~80%) demagnetization is Henry crater, putting a lower bound on dynamo cessation at 3.6 Ga. Although Lyot crater exhibits strong magnetization after the formation of Henry (3.4 Ga), we calculate Curie depths and impact-induced shock wave pressures to show that a previously existing magnetized layer could have persisted in spite of the impact, validating the 3.6 Ga dynamo cessation estimate. We also provide a generalized method/code for constraining the depth of magnetic sources within the crust at sites of heavy impact cratering, which can be extrapolated to larger surfaces to cross-validate spherical harmonic models through forward modeling of power spectra.

Outline

1. Background	2
2. Methods	3
2.1. Dynamo Cessation Estimate	3
2.2. Constraining Magnetization Depths	4
2.2.1. Lower Bound Calculation	4
2.2.2. Upper Boundary Calculation	5
3. Results and Discussion	7
3.1. Demagnetization Signatures	7
3.2. Magnetic Source Depths	10
4. Conclusion	12
5. Supplemental Information	12
6. References	13

Key Terms

1. **Dynamo** — The process by which a celestial body generates a global magnetic field, or magnetosphere, through the motion of electrically conducting fluids such as molten iron in its core. This magnetic field is then able to deflect charged particles from the Sun and other cosmic sources which would otherwise damage living organisms and erode surface water/atmosphere.
2. **Lithosphere** — The outermost shell of a terrestrial planet composed of rocks and minerals, including the crust and uppermost parts of the mantle. The lithosphere can be broken into tectonic plates that move/interact to cause earthquakes, magmatic intrusions, and volcanic eruptions. Note that this term can have several different meanings depending on the scope of the work.
3. **Ga** — Short for "giga-annums", which is a unit of a billion year (10^9).
4. **Thermal remanent magnetization (TRM)** — The process by which a material is heated past a characteristic temperature known as its Curie point and is remagnetized by a background magnetic field as it cools. At a molecular level, this occurs because the material's permanent magnetic dipole moments (electrons, in the case of iron-bearing minerals) have enough thermal energy to be disordered and randomized, losing any previously-existing overall dipole alignment that produce net magnetic fields. If an ambient field is present, these dipole moments have enough rotational freedom to be realigned with an amplitude/direction proportional to the ambient field.
5. **Shock wave** — Sudden and intense increases in pressure that travels through a medium with wave-like properties (i.e. exhibits constructive and destructive interference) as a result of a high-energy impact.
6. **Shock wave remanent magnetization (SRM)** — Similar to TRM, but the threshold is extreme pressures due to compression rather than heating.
7. **Impact crater** — A depression/hole/cavity formed on the surface of a planetary body as a result of an impact event, such as an asteroid or comet collision. The size and shape of the crater depend on various factors, including the size of the impactor, its velocity, and the type of material it impacts.
8. **Radiogenic heat-producing elements (HPEs)** — Isotopes of certain elements that produce heat as a byproduct of the natural radioactive decay of their nucleus. This drives various geodynamic processes, such as plate tectonics and volcanic activity, and contributes to the overall thermal evolution of a planetary body.

1. Background

[1] Planets in the solar system are constantly bombarded by cosmic radiation, primarily in the form of high-speed and high-energy solar winds, which can erode their atmosphere and be detrimental to living organisms under direct exposure. However, planets such as Earth which have a strong planetary-scale magnetic field (i.e. magnetosphere) generated by an active core (i.e. dynamo) are capable of deflecting these harmful cosmic radiation. In addition, the dynamo is closely tied to the structure and evolution of a planet's core, mantle, and lithosphere. Unlike Earth, Mars lacks a presently active dynamo which was first indicated by the Mariner IV fly-by in 1964 (Smith et al., 1965). As a result, living organisms and stable liquid water can't exist on the surface of Mars due to its extremely thin and cold atmosphere.

[2] In contrast to these observations, the presence of dried-up valley networks, sedimentary deposits, large flood channels, and polar ice caps on Mars provide compelling evidence that it used to have an ancient Earth-like dynamo that supported a thick atmosphere, expansive bodies of surface water, and possibly life (Orosei et al., 2020; Stevenson, 2001). This was confirmed by analyses of a fragmented Martian meteorite ALH84001 that landed on Earth, which seems to have been magnetized by a strong Martian dynamo 4 Ga (giga-annums, or billions of years) ago (Weiss et al., 2002). Since then, NASA's MGS orbiter (Mars Global Surveyor, 1997-2006), MAVEN orbiter (Mars Atmosphere and Volatile Evolution, 2014-present), and InSight lander (Interior Exploration using Seismic Investigations, Geodesy and Heat Transport, 2018-2022) have collected a plethora of orbital magnetic field measurements. This has enabled further analysis of the ancient dynamo, and by proxy, helped contextualize formative geological events on Mars.

[3] However, two major uncertainties remain. First, the precise timing of the dynamo's demise is still widely debated, with estimates ranging from 4.2-Ga (Early Noachian era) to 3.6-Ga (Early Hesperian era) as summarized in Figure 1. Many important geological events such as volcanism, major impact basins, and valley network activity occurred within this range of uncertainty,

so a clearer picture of the dynamo's evolution/demise will help us understand and contextualize early formative activity. Second, the depth of magnetic sources within the lithosphere is unknown for most of the surface. This information is key to discriminating between different crustal formation mechanisms and determining the time of magnetic acquisition.

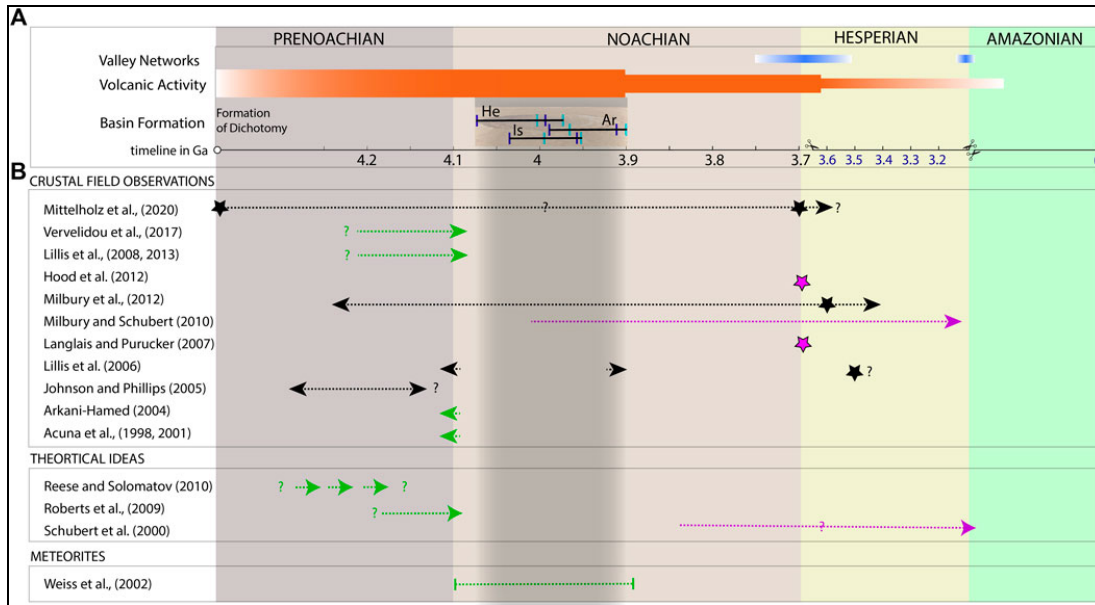


Figure 1: A summary timeline for (A) major relevant volcanic, fluvial activity and basin formation events on Mars, and (B) dynamo lifetime estimates from various literature sources (Mittelholz & Johnson, 2022) .

[4] In this work, we approach these two questions through the lens of magnetic field signatures around asteroid impact craters. This is because at the time of an asteroid impact, nearby iron-bearing minerals experience sudden intense compression and heating past a temperature known as the Curie point, which leads to net demagnetization. Critically, the mineral is then susceptible to being remagnetized as they settle and cool if a background magnetic field is present (such as the dynamo) in processes known as shock wave remanent magnetization (SRM) and thermal remanent magnetization (TRM). Minerals can preserve this acquired magnetization for billions of years, so studying them gives us a window into the planet's earliest conditions (Mittelholz et al., 2020). Notably, meteorite impacts cause sudden demagnetization and SRM/TRM as opposed to the slow, enigmatic TRM of volcanic processes, so impacts serve as a kind of "snapshot" of the dynamo-state at the time of formation.

2. Methods

2.1. Dynamo Cessation Estimate

[5] NASA's MAVEN satellite has been collecting data from Mars's orbit from 2014 to present day. MAVEN's magnetometers can measure the crustal magnetic field at altitudes as low as 130 km with high resolution, allowing us to detect signals that were too weak or had wavelengths too short to be observed by MGS. Additionally, global nighttime data at altitudes under 200 km cover 93% of Mars as opposed to the <20% coverage of MGS. Vector magnetic field data acquired by the Fluxgate Magnetometers aboard the MAVEN spacecraft can be downloaded from the NASA Planetary Data System website (Jack Connerney, 2017). We limit our scope to data altitudes less than 200 km. We also only consider nighttime data (collected from 20:00—09:00) because solar wind interactions in the daytime near-surface induce electric currents in Mars's ionosphere which generate their own magnetic fields, introducing long-wave biases that muddle and intensify MAVEN's measurements of sunny terrain.

[6] To systematically search through craters, we use a comprehensive global database of Mars impact craters ≥ 1 km in diameter (Hynek et al., 2010). We extract the information for craters with diameters between 70-500 km, which gives us a sample size of 855 total craters (754 between 70-150 km, 83 between 150-300 km, 18 between 300-500 km). For each crater, we first isolate MAVEN data points in/around the crater, and then sort these data into the individual tracks they originated from according to abrupt jumps in latitude. The crustal magnetic field components/magnitude and satellite altitude for each track are then plotted against latitude with/without linear detrending (meaning we subtract each track's best fit linear regression line).

[7] With cross-sectional plots for all 855 craters, we narrow or focus on craters for which the time of formation can be determined. This information is partially provided by Lillis et al., 2013, and we replicate the sub-cratering density methods to estimate the age of additional craters of interest that show clear remagnetization/demagnetization signatures. With this reduced sample of 17 craters, we assign a subjective crustal magnetization rating from -3 (strong demagnetization), to 0 (ambiguous), to +3 (strong magnetization), then plot these against the age of the crater.

2.2. Constraining Magnetization Depths

[8] Having established a chronology and estimation of real crustal magnetization for each crater based on magnetometer data, we develop a theoretical validation model by analyzing other geophysical processes in order to constrain the range of depths at which magnetic sources can reside in the lithosphere. For the lower bound, we know that minerals can't retain magnetization below the "Curie depth" where the decay of radioactive elements produces enough heat to exceed a mineral's Curie point. For the upper bound, we calculate the extent of impact-induced shock wave demagnetization.

2.2.1. Lower Bound Calculation

[9] Temperatures tends to progressively increase with proximity to the core of planetary bodies. By analytically solving the one-dimensional form of Fourier's law of heat conduction $\left(q = -k \frac{dT}{dz}\right)$ with the appropriate boundary conditions at the surface/lithosphere/mantle, we can determine the temperature as a function of depth underneath the surface in order to find Curie depths, or the depth past which no magnetization can exist in certain iron-bearing minerals. If we assume heat is exclusively produced from within the crust (i.e. the mantle is depleted in heat-producing elements (Ojha et al., 2019)) and transferred from the lower mantle to the base of the lithosphere, the equation for 1D steady heat conduction with volumetric heat production is given by the following equation,

$$T(z, \theta, \phi, t) = \begin{cases} \frac{\rho \cdot H(\theta, \phi, t) \cdot z}{\kappa_c} \left(z_{\text{crust}}(\theta, \phi) - \frac{z}{2} \right) + \frac{q_b z}{\kappa_c} & , \{z < z_{\text{crust}}\} \\ T_0 + \frac{\rho \cdot H(\theta, \phi, t) \cdot z_{\text{crust}}(\theta, \phi)^2}{2\kappa_m} + \frac{q_b z}{\kappa_m} & , \{z > z_{\text{crust}}\} \end{cases} \quad (1)$$

where z is depth below the surface; ρ is density of the crust which we set to $2,800 \text{ kg} \cdot \text{m}^{-3}$ (Ojha et al., 2020); κ_c and κ_m are thermal conductivities of the crust and mantle which we set to 2.5 and $4 \text{ W} \cdot \text{m}^{-1} \cdot \text{K}^{-1}$ (Schumacher & Breuer, 2006); q_b is the heat flow from the lower mantle to the base of the lithosphere which we set to 15 mW according to prior estimates of ancient Mars based on lithospheric deflection (Ojha et al., 2019); T_0 is a correction term to ensure continuity at the boundary between crust and mantle; and $z_{\text{crust}}(\theta, \phi)$ is the thickness of the crust at a certain longitude/latitude as determined by gravity data (Gong & Wiczorek, 2021).

[10] The final term in equation 1 is $H(\theta, \phi, t)$, or heat production per unit mass, whose calculation is more involved as a function of position and time. Conceptually, the lithosphere of Mars contains certain radioactive isotopes ^{235}U , ^{238}U , ^{232}Th , and ^{40}K which produce upward-flowing heat as they decay over time. This accounts for the majority of conductive heat loss to the surface for both Mars and Earth. The equation for H is given by

$$H(\theta, \phi, t) = \sum_X f_X \cdot C_X(\theta, \phi) \cdot H_X \cdot \left(\frac{t \cdot \ln 2}{\tau_X} \right), \quad (2)$$

for $X \in \left\{ {}^{235}\text{U}, {}^{238}\text{U}, {}^{232}\text{Th}, {}^{40}\text{K} \right\}$, where f_X is the isotopic fraction of element X ; H_X is the heat release rate constant of element X ; and τ_X is the half-life of element X . All three of these values are well-defined constants discussed in numerous prior works (Hahn et al., 2011; Ojha et al., 2020; Turcotte, 2014). The first dependent variable in equation 2 is t , which is how long ago we wish to calculate H relative to present day (this is necessary because radioactive heat-producing elements will decrease in abundance from their initial concentrations over time as they decay). This t is taken to be the previously determined time of formation of a crater.

[11] The second dependent quantity in equation 2 is $C_X(\theta, \phi)$, which represents the concentration by mass of element X at some position. To get this value, we used $5^\circ \times 5^\circ$ chemical abundance maps of the Martian shallow subsurface derived from spectroscopy by the Mars Odyssey Gamma Ray Spectrometer (GRS) Suite (Boynton et al., 2007). Specifically, we extract near-surface elemental concentrations of K and Th at the four "pixels" closest to the crater, and use weighted bilinear interpolation to estimate the concentrations at the exact coordinates of the crater. The elemental concentration of U can then be calculated using a cosmochemically constant Th / U mass ratio of 3.8. At this point, it's important to note that the GRS chemical maps only represent the top tens of centimeters of Martian surface, and are therefore heavily influenced by near-surface regolith, ice, and dust deposits. However, previous studies provide strong reasons in defense of vertically homogeneous distribution of these heat producing elements given certain adjustments (Boynton et al., 2007; Taylor et al., 2006). To make these K, Th, and U measurements accurately represent the bulk chemistry of the entire Martian upper lithosphere, we must renormalize our values to a volatile-free basis. This is done by using the same methods and data suite to extract near-surface elemental concentrations of Cl, H_2O , and S at the desired coordinate, summing these to find the net concentration by mass of volatiles denoted as V , and then multiplying the K, Th, and U measurements by $\frac{1}{1-V}$ each. We note that at high latitudes, water ice saturating regolith pore space overwhelms the signatures of other elements in gamma spectra, preventing GRS instruments from collecting meaningful data.

[12] We now have a complete procedure for calculating a temperature versus depth profile for the lithosphere at a specific location and time in the past. In order to find points of potential demagnetization, we identify the three primary iron-bearing minerals which carry the bulk of magnetization within the lithosphere and their associated Curie temperatures T_C , which are well-defined in prior works: single domain magnetite Fe_3O_4 with $T_C = 580^\circ\text{C}$; single domain pyrrhotite Fe_{1-x}S for $x < 0.13$ with $T_C = 320^\circ\text{C}$; and multidomain hematite Fe_2O_3 with $T_C = 670^\circ\text{C}$ (Artemieva et al., 2005).

2.2.2. Upper Boundary Calculation

[13] Meteor impacts deliver high amounts of energy which can demagnetize the nearby crust by three main processes. First, an impact can excavate a large cavity and displace (possibly magnetized) crust over a large region with random orientation. Second, the impact-induced shock wave can create high pressure which demagnetizes minerals. Third, the impact kinetic energy is converted to heat which can exceed the Curie temperatures of underlying minerals which leads to demagnetization. In the latter two cases, directly following demagnetization, minerals are susceptible to being remagnetized by a possible ambient field such as the dynamo as they settle/cool. These processes are known as shock wave remanent magnetization (SRM) and thermal remanent magnetization (TRM) respectively. However, this remagnetization does not occur in the absence of a dynamo field, meaning the affected minerals remain demagnetized.

[14] These three demagnetization processes are the likely explanation for the absence of crustal magnetic field signatures over the giant basins of Mars (Acuña et al., 1999). However, for smaller impacts (<500 km), there may not be sufficient energy to affect the magnetized layer in the crust which could be buried several tens of kilometers beneath the surface. In these cases, we

calculate impact-induced shock pressure using modified Holsapple-Schmidt-Housen laws (Mohit & Arkani-Hamed, 2004; Shahnas & Arkani-Hamed, 2007) to estimate the extent of crustal demagnetization. We do not consider heat-induced thermal demagnetization because its spatial extent is likely less than that of shock demagnetization (Mohit & Arkani-Hamed, 2004).

[15] The only crater-dependent input in our calculations is the observed crater diameter, D_o . From this, we find the transient crater diameter D_{tr} , or the diameter of the crater immediately after impact but before undergoing collapse and modification, with

$$D_{tr} = 0.7576 \cdot D_o^{0.921} \cdot D_*^{0.079}, \quad (3)$$

where D_* is the transition diameter from simple to complex crater, assumed 7 km for Mars (Melosh, 1989). We use this to find the kinetic energy E of the projectile immediately before impact with

$$E = \left[(D_{tr} \cdot v^{0.09} \cdot g^{0.22}) / 0.2212 \right]^{(1/0.26)}. \quad (4)$$

The majority of impact craters on Mars are formed by heliocentric projectiles with velocity 8 – 12 km/s (Neukum & Wise, 1976), so we set the impactor speed $v = 10$ km/s. The gravitational acceleration at the surface of Mars is $g = 3.721$ m/s.

[16] We assume the projectile is a sphere ($V = \frac{4}{3}\pi r^3$) of basaltic composition density ($\rho = 2,900$ kg/m³) and kinetic energy $E = \frac{1}{2}Mv^2$. This allows us to solve the density relation $\rho = M/V$ for the radius of the projectile,

$$r_{\text{proj}} = \left(\frac{3E}{2\pi\rho v^2} \right)^{1/3}. \quad (5)$$

[17] We are now ready to begin defining the pressures associated with the impact. First, we consider a region associated with hypervelocity impacts known as the isobaric core, where the pressure is nearly constantly. The spatial extent of this region is known as the isobaric radius, which is about 75% of the impactor radius ($R_0 = 0.75 \cdot r_{\text{proj}}$) (Mohit & Arkani-Hamed, 2004). The pressure P_0 within the isobaric core is derived from the Hugoniot equation, which works out to be

$$\begin{aligned} P_0 - P'_0 &= \rho \cdot v_p \cdot v_s \\ &= \rho \cdot v_p \cdot (C + sv_p) \\ P_0 &= \frac{1}{4}\rho v(2C + sv). \end{aligned} \quad (6)$$

The shock wave velocity is simplified with $v_s = C + sv_p$. We take $C = 3.5$ km/s as the bulk speed of sound and $s = 1.5$ as the shock parameters of the target material, for which we use values for typical major crustal rocks (Melosh, 1989, Table AII.2).

We assume that particle velocity in the isobaric core is half the impactor velocity ($v_p = \frac{1}{2}v$) because the physical properties of the target and projectile are almost identical (Melosh, 1989).

[18] With these quantities, we define a supplementary function to calculate shock wave pressures:

$$P_{\text{naive}}(r) = \begin{cases} P_0 & \{r < R_0\} \\ \frac{1}{4}\rho v \left(2C + sv \left(\frac{R_0}{r} \right)^n \right) \left(\frac{R_0}{r} \right)^n & \{r > R_0\} \end{cases} \quad (7)$$

where we set $n = 1.87$ based on the constant exponent decay model described by Melosh, 1989.

[19] For our final calculation of effective pressure, we must account for the pressure reduction near the surface due to interference between direct and reflected shock waves. The distances traveled by direct and reflected waves at some point are respectively are given by

$$\begin{cases} R_{\text{direct}}(r, z) = \sqrt{(z - R_0)^2 + r^2} \\ R_{\text{reflect}}(r, z) = \sqrt{(z + R_0)^2 + r^2}, \end{cases} \quad (8)$$

where r is the horizontal distance (i.e. surface distance) and z is the vertical distance (i.e. depth) between the center of impact and a point. The time delay between the arrival of the initial and reflected shock waves is given by

$$\tau_{\text{delay}} = (R_{\text{reflect}} - R_{\text{direct}}) / C, \quad (9)$$

and the time it takes for the impact to reach maximum force is

$$\tau_{\text{rise}} = r_{\text{proj}} / v. \quad (10)$$

[20] Finally, we can find the effective pressure at some point underneath an impact:

$$P_{\text{eff}} = \begin{cases} P_{\text{naive}}(R_{\text{direct}}) & \{\tau_{\text{delay}} > \tau_{\text{rise}}\} \\ P_{\text{naive}}(R_{\text{direct}}) - P_{\text{naive}}(R_{\text{reflect}}) \cdot \left(1 - \frac{\tau_{\text{delay}}}{\tau_{\text{rise}}}\right) & \{\tau_{\text{delay}} < \tau_{\text{rise}}\} \end{cases}. \quad (11)$$

[21] Prior work analyzing the magnetic signatures and calculated distribution of shock pressures surrounding the giant impact basins Hellas, Isidis, and Argyre shows that the crust is almost completely demagnetized at pressures $\sim 2 - 3$ GPa (Mohit & Arkani-Hamed, 2004). We assume complete demagnetization at pressures of 2 GPa.

3. Results and Discussion

3.1. Demagnetization Signatures

[22] Previous works using analytical methods for impact-modeling predict that only craters with diameter greater than 300 km should produce detectable demagnetization signatures (Shahnas & Arkani-Hamed, 2007). However, recent work verified by our own analysis has suggested MAVEN can detect demagnetization signatures in impact craters as small as 70 km in regions such as Lucus Planum (Mittelholz et al., 2020). And yet, although our method of individual MAVEN track analysis is able to resolve more instances of demagnetization relative to lower-resolution MGS data, we still only observe demagnetization in $\sim 10\%$ of craters > 300 km diameter and $< 5\%$ of craters 150—300 km diameter. Among these, no statistically significant correlations were observed between location, eccentricity, or diameter of the crater. The majority of craters exhibit a constant magnetic field strength that does not vary across the impact radius (such as Figure 2). However, there are some notable examples such as Henry crater (pictured in Figures 3 and 4) which exhibits $\sim 85\%$ demagnetization despite a relatively small diameter of 167 km compared to other craters in this study.

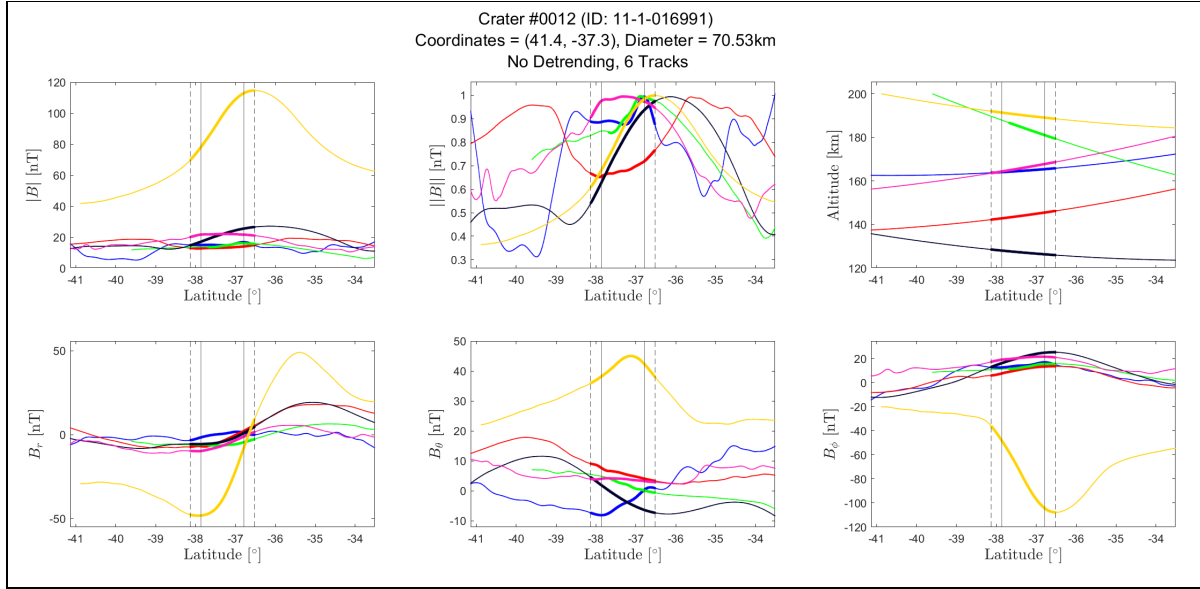


Figure 2: Magnetic field data over an unnamed crater. Bottom row: B_r , B_θ , and B_ϕ (spherical vector components of the magnetic field). Top row: $|B|$ (magnitude of the magnetic field), $||B||$ (magnitude of the magnetic field where each track is individually normalized to its maximum value), and Altitude (of the MAVEN satellite at the time of measurement). The solid and dashed lines represent the crater radius and $1.5\times$ the crater radius respectively. The "flatness" of the $|B|$ plot indicates the absence of any impact-induced magnetic anomalies at this crater. The yellow track appears to be an outlier, but this can be attributed to noise due to high altitude and random space weather creating disruptions in the ionosphere.

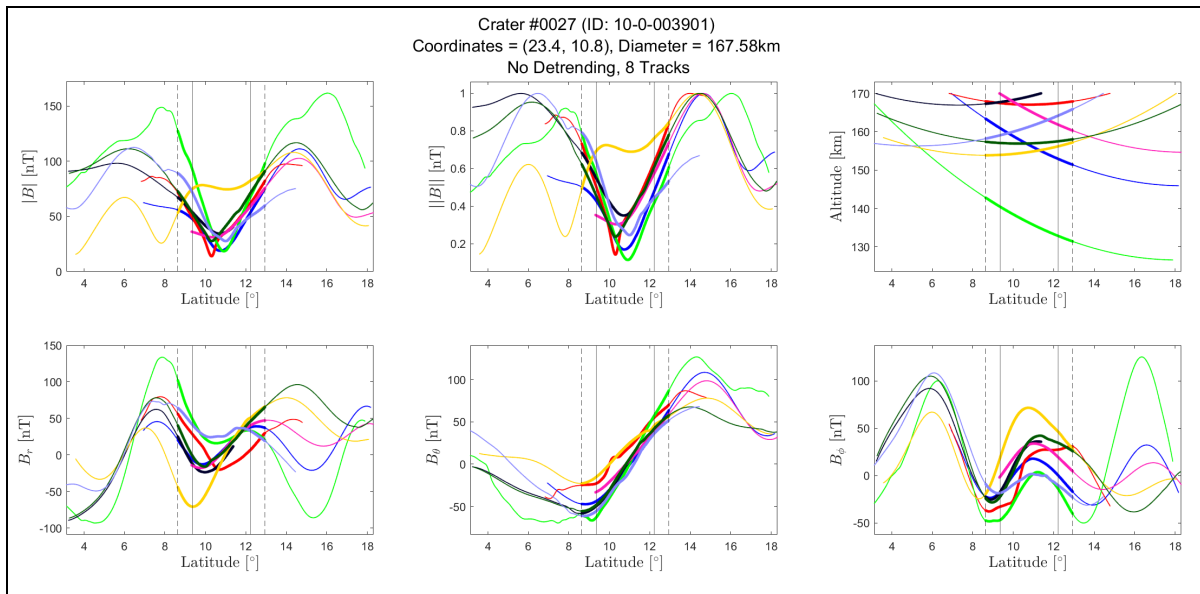


Figure 3: Magnetic field data over Henry crater. The strong "dip" in $|B|$ and $||B||$ as the tracks pass through the crater and the fact that all spherical components cross 0 suggest strong impact-induced demagnetization by more than 80% of the original field. Additionally, there was enough data in this crater to reduce the maximum altitude from 200 km to 170 km, further increasing the resolution and confidence in our results.

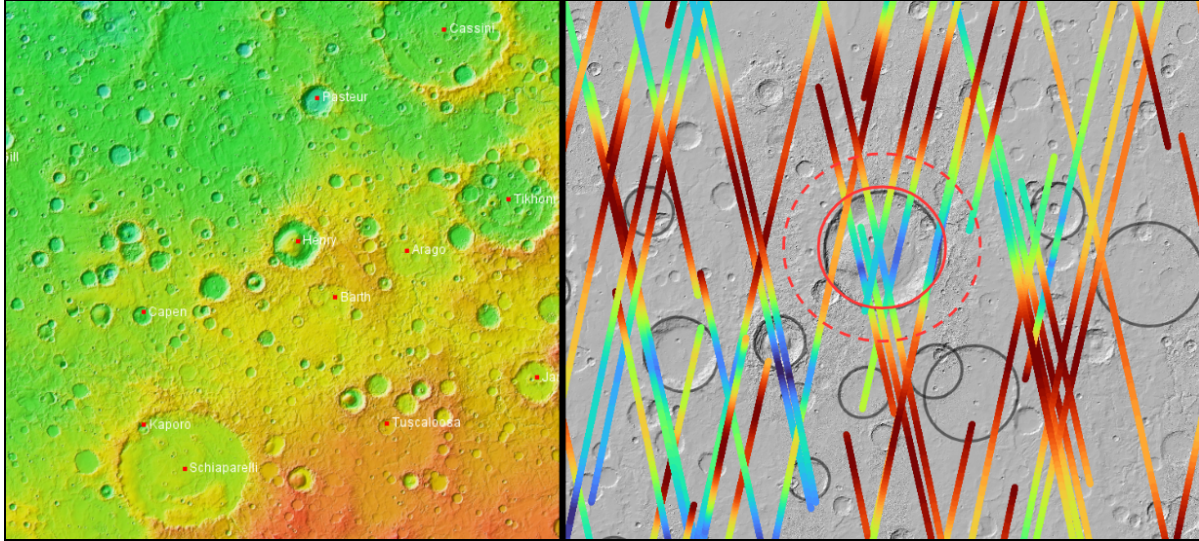


Figure 4: Geospatial visualization of Henry crater, whose cross-sectional magnetic field signatures are displayed in Figure 3. MOLA topography is shown on the left, and MAVEN's scalar magnetic field ($|B|$) measurements under 200 km altitude are shown on the right.

[23] The unambiguous demagnetization of Henry crater is most simply interpreted as a sign that the Martian dynamo had already shut down at the time of impact around 3.6 Ga, which is one of the primary conclusions of our work. This estimate sits at the boundary of some prior work but doesn't pose any serious contradictions, as illustrated in Figure 1. Naturally, this conclusion necessitates observed crustal demagnetization signatures in sufficiently large craters (minimum >70 km as observed in Lucus Planum; definitely >167 km as observed in Henry crater) younger than 3.6 Ga. However, when we attempt to correlate the magnetization ratings of craters with their age in Figure 5, we observe an ambiguous case of strong magnetization (10-50 nT) in the form of Lyot crater (220 km diameter) at ~3.4 Ga, with cross-sectional plots given in Figure 6.

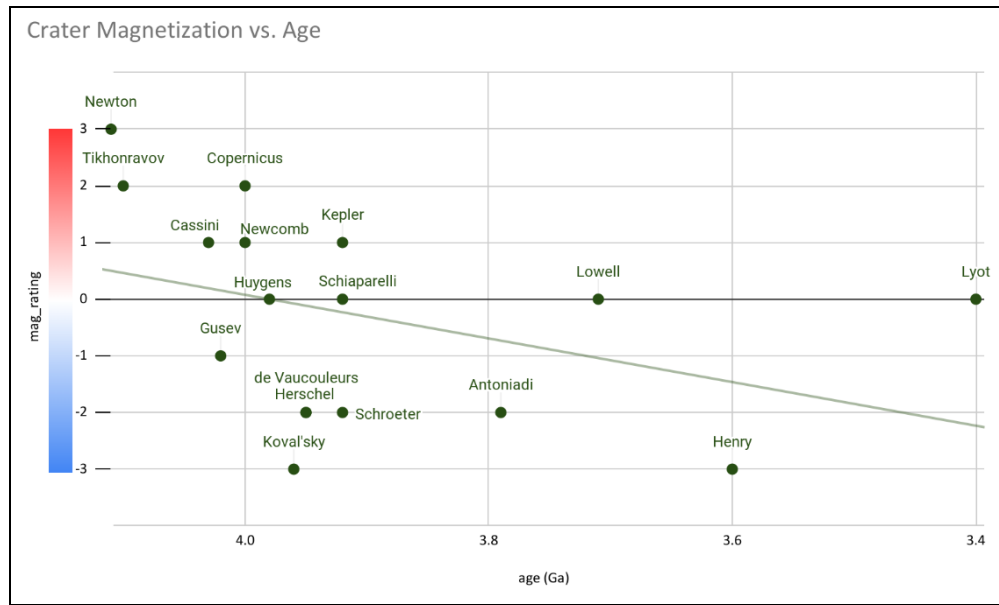


Figure 5: Age (in billions of years) versus magnetization rating (from -3=demagnetized to +3=remagnetized) for the 17 aged craters in this study. Our work suggest the dynamo was inactive by the formation of Henry crater at 3.6 Ga.

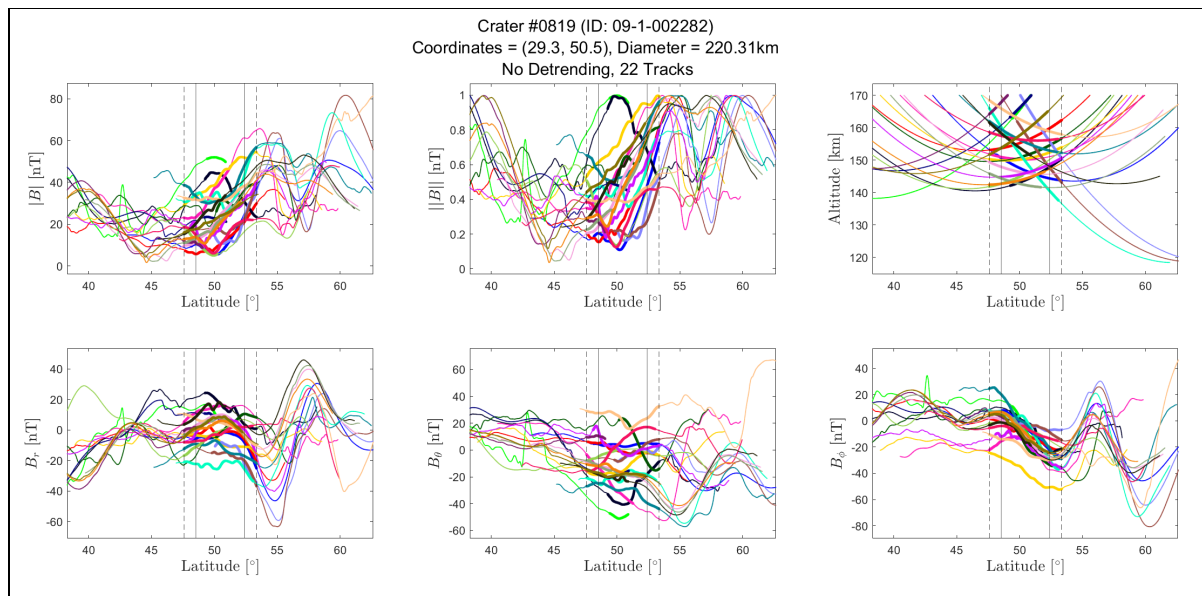


Figure 6: Magnetic field data over Lyot crater. Although we can't deduce any clear reduction/increase/constancy in field signatures, we observe the magnitude of the magnetic field $|B|$ ranges from 10–50 nT within the crater, which is inconsistent with an impact of this size occurring over an inactive dynamo.

3.2. Magnetic Source Depths

[24] One possible explanation for the persistence of strong crustal magnetization around Lyot crater is that the underlying magnetized layer is buried at a "sweet spot" that's deep enough to not be reached by impact-induced shock waves from the surface but shallow enough to be above the natural Curie depth. We write a generalized script that calculates these theoretical

upper/lower boundaries for a persistent magnetized layers at a given crater, and apply it to Lyot. We find that, at the time of impact, no magnetization could have persisted below a depth of 101 km (Figure 7) or above a depth of ~60 km (Figure 8). The upper bound is less certain because the spatial extent of demagnetization is rounded, but what matters is that there's a 40 km *minimum* region in the lithosphere that could maintain magnetic sources in spite of large impacts and the lack of a dynamo.

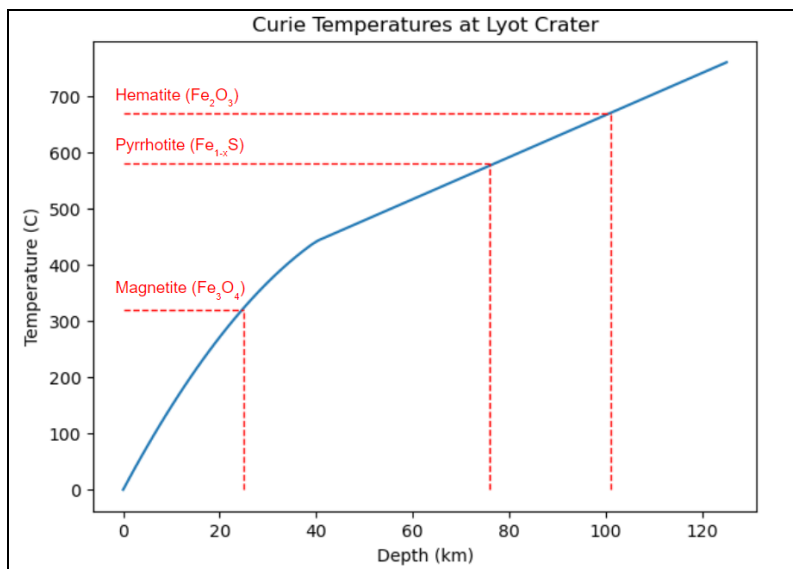


Figure 7: One-dimensional temperature versus depth profile of the lithosphere at time of impact for Lyot crater. Sources of heating are decay of radiogenic heat-producing elements and heat flow from the lower mantle to the base of the lithosphere. The horizontal red-dashed lines indicate the Curie temperatures of the three primary iron-bearing minerals which carry the bulk of magnetization within the lithosphere. The vertical red-dashed lines indicate the depth at which the Curie temperature is reached for each mineral (25 km, 76 km, and 101 km).

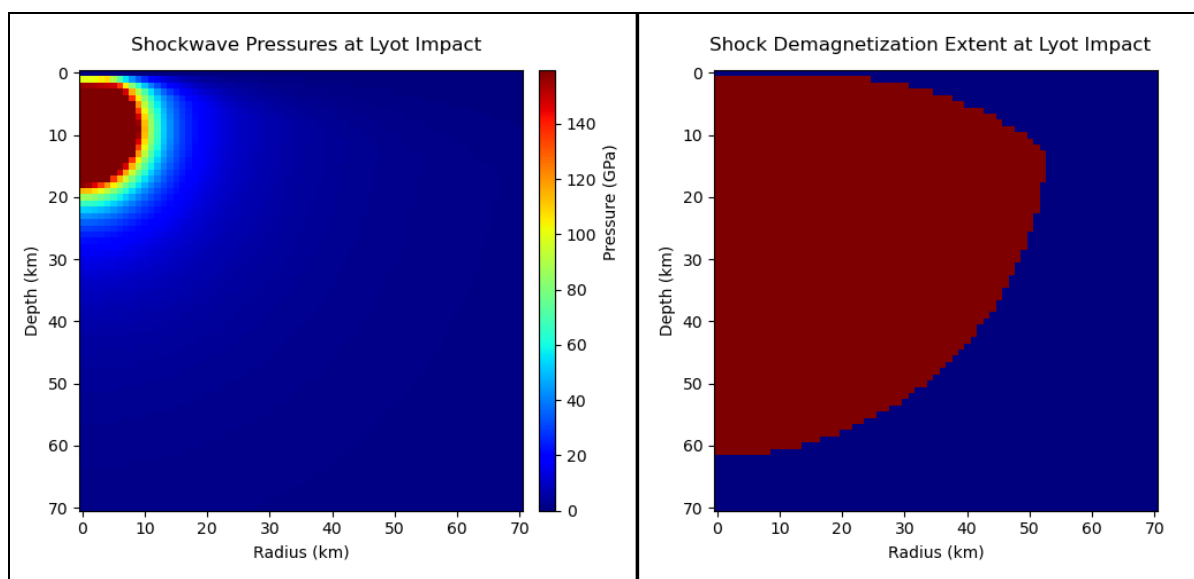


Figure 8: Spatial extents for impact-induced shock wave pressures (left) and demagnetization where pressures exceeding 2 GPa are colored red (right) in the lithosphere at the time of Lyot's impact.

4. Conclusion

[25] We analyze high-resolution crustal magnetic field data from MAVEN tracks in/around impact craters in the size range 70—500 km diameter. Demagnetization is only observed in ~10% of craters >300 km diameter and <5% of craters 150-300 km diameter, with no apparent correlations between location/size. We find a few compelling examples of extremely strong demagnetization, primarily in Henry crater (167 km diameter, age 3.6 Ga) located in the region Arabia Terra. From this, we conclude the Martian dynamo must have shut down before 3.6 Ga. Lyot initially challenges this theory since it appears to be a strongly magnetized crater younger than 3.6 Ga, but we find that magnetic sources could persist between 60-100km depths in spite of demagnetization from impact pressures and internal heat production, so our 3.6 Ga estimate holds.

[26] Putting a definite end of dynamo activity at 3.6 Ga gives important context to many events within the Hesperian era (3.7-3.0 Ga) by two primary mechanisms. The first is that processes which involve elevated heat and pressure would no longer be followed by remagnetization of local minerals. In other words, we expect demagnetization for both sudden (impacts) and long-lasting/enigmatic (radiogenic HPE decay, volcanic activity) events. The second is that the lack of a dynamo would allow solar winds to begin eroding the atmosphere and degrading water and organic materials on the surface. Furthermore, the fact that magnetic sources are deeply buried within the lithosphere indicate that magnetization was acquired during the formation of primordial crust or later as a result of magmatic intrusions. In contrast, shallow magnetic sources would suggest observed magnetization is primarily due to impact basin ejecta, surface pyroclastic flows, or impact melt sheets.

[27] The most direct next step would be to create a global map of average magnetic source depths using our analytical methods, and then attempt to validate that against models made from real MAVEN/MGS data. The latter models would be made by creating local spherical harmonic models of the magnetic field using altitude-cognizant scalar Slepian functions, performing spectral analysis, and then creating forward models of buried magnetic sources to find likely depths across the surface.

Assuming

these "real data" models are accurate, we can further adjust basal heating rates, volatile-normalization schemes for GRS data, and other parameters in our analytical model to see what it takes to bring it in line with the "real data" model, which may or may not lead to reasonable outcomes/assumptions/initial conditions that can be extrapolated to the whole of Mars.

[28] Demagnetization was previously thought to be completely predicated on the size of the crater and crustal excavation volume, but that doesn't seem to hold in our analysis. Applying the aforementioned magnetic source depth modeling as validation tests for specific impact craters could help us identify more variables that influence impact-induced demagnetization such as crustal thickness, variations in thermal conductivity, and more.

[29] Finally, our methods can be repeated with higher resolution datasets/models for more clear results. First, this study considers 17 craters, but that can be increased as more advanced crater dating techniques are developed to further narrow the range of dynamo activity. Second, analyzing individual MAVEN tracks often leads to incoherent field signatures (i.e. two measurements of the same location could show completely different values/trends), so better spherical harmonic models would help us see small fluctuations. Third, more sophisticated methods of calculating impact-induced shock wave pressures using finite element simulations such as iSale2D could account for more crustal/atmospheric composition parameters such as hydration, density, and layering via aeolian deposition. Fourth, our calculations of heat production/flow could be improved with more complex models that account for how certain parameters vary with depth such as thermal conductivity, lithosphere deflection due to topographical loads, and magmatic intrusions.

5. Supplemental Information

The processed data used in our analysis and MATLAB/Python code used to generate it is available in the following GitHub repository: <https://github.com/Humboldt-Penguin/Mars-Magnetics-Research>.

6. References

- Acuña, M. H., Connerney, J. E. P., F., N., Ness, Lin, R. P., Mitchell, D., Carlson, C. W., McFadden, J., Anderson, K. A., Rème, H., Mazelle, C., Vignes, D., Wasilewski, P., & Cloutier, P. (1999). Global Distribution of Crustal Magnetization Discovered by the Mars Global Surveyor MAG/ER Experiment. *Science*, 284(5415), 790–793. <https://doi.org/10.1126/science.284.5415.790>
- Artemieva, N., Hood, L., & Ivanov, B. A. (2005). Impact demagnetization of the Martian crust: Primaries versus secondaries. *Geophysical Research Letters*, 32(22), n/a-n/a. <https://doi.org/10.1029/2005gl024385>
- Boynton, W. V., Taylor, G. J., Evans, L. G., Reedy, R. C., Starr, R., Janes, D. M., Kerry, K. E., Drake, D. M., Kim, K. J., Williams, R. M. S., Crombie, M. K., Dohm, J. M., Baker, V., Metzger, A. E., Karunatillake, S., Keller, J. M., Newsom, H. E., Arnold, J. R., Brückner, J., ... Hamara, D. K. (2007). Concentration of H, Si, Cl, K, Fe, and Th in the low- and mid-latitude regions of Mars. *Journal of Geophysical Research*, 112(E12). <https://doi.org/10.1029/2007je002887>
- Gong, S., & Wicczorek, M. (2021). Depth of Martian Magnetization From Localized Power Spectrum Analysis. *Journal of Geophysical Research: Planets*, 126(8). <https://doi.org/10.1029/2020je006690>
- Hahn, B. C., McLennan, S. M., & Klein, E. C. (2011). Martian surface heat production and crustal heat flow from Mars Odyssey Gamma-Ray spectrometry. *Geophysical Research Letters*, 38(14), n/a-n/a. <https://doi.org/10.1029/2011gl047435>
- Hynek, B. M., Beach, M., & Hoke, M. R. T. (2010). Updated global map of Martian valley networks and implications for climate and hydrologic processes. *Journal of Geophysical Research*, 115(E9). <https://doi.org/10.1029/2009je003548>
- Jack Connerney. (2017). *MAVEN Tabulated vector magnetic field vs. time in planetocentric coordinates Data Collection* [Data set]. NASA Planetary Data System. <https://doi.org/10.17189/1414247>
- Lillis, R. J., Robbins, S., Manga, M., Halekas, J. S., & Frey, H. V. (2013). Time history of the Martian dynamo from crater magnetic field analysis. *Journal of Geophysical Research: Planets*, 118(7), 1488–1511. <https://doi.org/10.1002/jgre.20105>
- Melosh, H. J. (1989). Impact cratering: A geologic process. *New York: Oxford University Press; Oxford: Clarendon Press.*
- Mittelholz, A., Johnson, C. L., Feinberg, J. M., Langlais, B., & Phillips, R. J. (2020). Timing of the martian dynamo: New constraints for a core field 4.5 and 3.7 Ga ago. *Science Advances*, 6(18). <https://doi.org/10.1126/sciadv.aba0513>
- Mittelholz, Anna, & Johnson, C. L. (2022). The Martian Crustal Magnetic Field. *Frontiers in Astronomy and Space Sciences*, 9. <https://doi.org/10.3389/fspas.2022.895362>
- Mohit, P. S., & Arkani-Hamed, J. (2004). Impact demagnetization of the martian crust. *Icarus*, 168(2), 305–317. <https://doi.org/10.1016/j.icarus.2003.12.005>
- Neukum, G., & Wise, D. (1976). Mars: A Standard Crater Curve and Possible New Time Scale: Cratering links to lunar time suggest that Mars died long ago. *Science*, 194(4272), 1381–1387.
- Ojha, L., Buffo, J., Karunatillake, S., & Siegler, M. (2020). Groundwater production from geothermal heating on early Mars and implication for early martian habitability. *Science Advances*, 6(49). <https://doi.org/10.1126/sciadv.abb1669>
- Ojha, L., Karimi, S., Lewis, K. W., Smrekar, S. E., & Siegler, M. (2019). Depletion of Heat Producing Elements in the Martian Mantle. *Geophysical Research Letters*, 46(22), 12756–12763. <https://doi.org/10.1029/2019gl085234>
- Orosei, R., Ding, C., Fa, W., Giannopoulos, A., Hérique, A., Kofman, W., Lauro, S. E., Li, C., Pettinelli, E., Su, Y., Xing, S., & Xu, Y. (2020). The Global Search for Liquid Water on Mars from Orbit: Current and Future Perspectives. *Life*, 10(8), 120. <https://doi.org/10.3390/life10080120>
- Schumacher, S., & Breuer, D. (2006). Influence of a variable thermal conductivity on the thermochemical evolution of Mars. *Journal of Geophysical Research: Planets*, 111(E2), n/a-n/a. <https://doi.org/10.1029/2005je002429>

- Shahnas, H., & Arkani-Hamed, J. (2007). Viscous and impact demagnetization of Martian crust. *Journal of Geophysical Research*, 112(E2). <https://doi.org/10.1029/2005je002424>
- Smith, E. J., Davis, L., Jr., Coleman, P. J., Jr., & Jones, D. E. (1965). Magnetic Field Measurements near Mars. *Science*, 149(3689), 1241–1242. <https://doi.org/10.1126/science.149.3689.1241>
- Stevenson, D. J. (2001). Mars' core and magnetism. *Nature*, 412(6843), 214–219. <https://doi.org/10.1038/35084155>
- Taylor, G. J., Boynton, W., Brückner, J., Wänke, H., Dreibus, G., Kerry, K., Keller, J., Reedy, R., Evans, L., Starr, R., Squyres, S., Karunatillake, S., Gasnault, O., Maurice, S., d'Uston, C., Englert, P., Dohm, J., Baker, V., Hamara, D., ... Drake, D. (2006). Bulk composition and early differentiation of Mars. *Journal of Geophysical Research*, 112(E3). <https://doi.org/10.1029/2005je002645>
- Turcotte, D. L. (2014). *Schubert, and Schubert, G.: Geodynamics*. Cambridge University Press, Cambridge.
- Weiss, B. P., Vali, H., Baudenbacher, F. J., Kirschvink, J. L., Stewart, S. T., & Shuster, D. L. (2002). Records of an ancient Martian magnetic field in ALH84001. *Earth and Planetary Science Letters*, 201(3–4), 449–463. [https://doi.org/10.1016/s0012-821x\(02\)00728-8](https://doi.org/10.1016/s0012-821x(02)00728-8)